Mechanical and functional characterisation of a 3D porous biomimetic extracellular matrix to study insulin secretion from pancreatic β-cell lines

Leonid Pliner, Nathan Laneret, Meryl Roudaut, Alejandra Mogrovejo-Valdivia, Elodie Vandenhaute, Nathalie Maubon, Robert-Alain Toillon, Youness Karrout, Anthony Treizebre, Jean-Sébastien Annicotte

In vitro models
https://doi.org/10.1007/s44164-024-00078-z

ORIGINAL RESEARCH

Mechanical and functional characterisation of a 3D porous biomimetic extracellular matrix to study insulin secretion from pancreatic β-cell lines

Leonid Pliner[1] · Nathan Laneret[2] · Meryl Roudaut[3] · Alejandra Mogrovejo-Valdivia[3] · Elodie Vandenhaute[3] · Nathalie Maubon[3] · Robert-Alain Toillon[2] · Youness Karrout[4] · Anthony Treizebre[5] · Jean-Sébastien Annicotte[1]

Received: 7 June 2024 / Revised: 27 September 2024 / Accepted: 30 September 2024

Abstract

Background Extracellular matrix (ECM) is a three-dimensional (3D) structure found around cells in the tissues of many organisms. It is composed mainly of fibrous proteins, such as collagen and elastin, and adhesive glycoproteins, such as fibronectin and laminin—as well as proteoglycans, such as hyaluronic acid. The ECM performs several essential functions, including structural support of tissues, regulation of cell communication, adhesion, migration, and differentiation by providing biochemical and biomechanical cues to the cells. Pancreatic β-cells have been previously shown to be responsive to the surrounding mechanical stress, impacting their insulin-secreting function.

Purpose We aimed to derive a physiologically relevant in vitro model of pancreatic tissue by using an innovative synthesised porous ECM that mimics the native tissue microenvironment and mechanical properties.

Methods Here we performed mechanical, physico-chemical and functional characterisation of a synthetic hydrogel ECM, composed of hyaluronic acid cross-linked with collagen types I and VI and modified with fibronectin. The hydrogel was used as a 3D cell culture scaffold for the MIN6 insulinoma cell line. Cell proliferation, viability, gene expression, and insulin secretion in response to glucose stimulus were assessed and contrasted with classic monolayer culture.

Results The biomaterial exhibited a shear modulus of 815.37 kPa and a distinctive viscoelastic response. MIN6 cells showed a higher proliferation and viability rates and maintained insulin secretion in response to glucose stimulus and β-cell identity gene expression when cultured in the 3D hydrogel compared to monolayer culture.

Conclusion Our study demonstrated the potential of this biomimetic hydrogel scaffold as an innovative matrix enabling better in vitro models to study disease physiopathology.

Keywords Biomaterial · Extracellular matrix · 3D cell culture · Pancreatic β-cells

Anthony Treizebre and Jean-Sébastien Annicotte are co-senior authors.

✉ Jean-Sébastien Annicotte
jean-sebastien.annicotte@inserm.fr

Anthony Treizebre
anthony.treizere@univ-lille.fr

[1] Univ. Lille, Inserm, CHU Lille, Institut Pasteur Lille, U1167 - RID-AGE - Facteurs de Risque Et Déterminants Moléculaires Des Maladies Liées Au Vieillissement, F-59000 Lille, France

[2] Univ. Lille, CNRS, Inserm, CHU Lille, UMR9020-U1277 – CANTHER – Cancer Heterogeneity Plasticity and Resistance to Therapies, 59000 Lille, France

[3] HCS Pharma, 59000 Lille, France

[4] Univ. Lille, Inserm, CHU Lille, U1008, F-59000 Lille, France

[5] Univ. Lille, CNRS, Univ Polytechnique Hauts-de-France, Junia, UMR 8520 - IEMN – Institut d'Électronique de Microélectronique et de Nanotechnologie, F-59000 Lille, France

Published online: 25 October 2024

Introduction

Diabetes mellitus, a chronic metabolic disorder characterised by hyperglycaemia, affects millions of people worldwide. While type 1 diabetes (T1D) results from autoimmune destruction of pancreatic β-cells, type 2 diabetes (T2D) is associated with insulin resistance of peripheral tissues such as muscle, liver, adipose tissue, and progressive loss of β-cell mass and function [1]. Pancreatic islet transplantation has emerged as a promising treatment for T1D [2], which gave rise to the development of porous scaffold grafts to enhance long-term survival and function of the transplanted islets [3]. Moreover, the development of effective therapies for T2D requires a better understanding of the mechanisms underlying pancreatic β-cell dysfunction, which can be facilitated by advanced in vitro models [4].

The extracellular matrix (ECM) plays a crucial role in providing structural support and regulating cellular behaviour, growth, and differentiation in living tissues [5, 6]. ECM is a complex network of proteins and polysaccharides that exhibits viscoelastic mechanical properties, which are essential for tissue-specific functions [7–9]. The influence of ECM on pancreatic islet cell differentiation, attachment, and proliferation has been well-established [10, 11], highlighting the need for incorporating ECM components in three-dimensional (3D) in vitro models to improve their relevance and predictive power.

Current in vitro models of pancreatic islets involve synthetic polymer matrices, such as polyethylene glycol (PEG), polylactic acid (PLA), and poly(lactic-co-glycolic acid) (PLGA) [12]. These materials often lack the complexity and biomechanical cues provided by the native ECM, leading to limitations in their ability to recapitulate the in vivo behaviour of islet cells. Various strategies, such as protein hydrogels, scaffolds, and decellularised matrices, have been employed to address this issue. For instance, Daoud et al. demonstrated that the presence of ECM components, such as collagen and laminin, improved the survival and function of human islets in vitro. Nagata et al. showed that culturing rat islets in an ECM-derived scaffold enhanced insulin secretion compared to conventional culture methods [13–18]. However, there remains a need for a more comprehensive and biomimetic approach that combines the key structural and functional components of the ECM to enhance the performance of in vitro islet models.

In this study, we aimed to bridge the gap between current in vitro models and the native islet microenvironment by developing a synthesised biomimetic scaffold that serves as an extracellular matrix for 3D cell culture. By incorporating key ECM components, such as fibrous proteins (collagen types I and VI), proteoglycans (hyaluronic acid, HA), and adhesive glycoproteins (fibronectin), we sought to provide the necessary biomechanical cues and cell–matrix interactions that are essential for maintaining pancreatic β-cell function and viability [19, 20]. By fine-tuning the composition and structure of our synthesised scaffold, we aimed to achieve viscoelastic properties that closely mimic the native tissue, thus providing an optimal microenvironment for islet cell function.

Our work focused on MIN6 cells, a well-established mouse pancreatic β-cell line, relatively easy to maintain and capable of robust insulin secretion in response to glucose stimulus. We used this cell line to validate the performance of the synthesised biomimetic scaffold as a model for studying glucose-stimulated insulin secretion [21, 22]. By comparing the behaviour of MIN6 cells cultured in our 3D scaffold with those in conventional two-dimensional (2D) cultures, we aimed to evaluate cell metabolic activity and insulin secretion in response to glucose stimulation.

Materials and methods

Hydrogel scaffold fabrication

The hydrogel scaffold was prepared as previously described [23]. Briefly, the BIOMIMESYS® Adipose Tissue scaffolds were synthesised in two steps. Initially, HA (9067–32-7, Baoding Faithful Industry Co., Ltd, China) was completely dissolved in pure water at the concentration of 4 g/L, followed by the addition of 10 mg of Arg-Gly-Asp-Ser motif (RGDS, 91,037–65-9, Cayman Chemicals, USA), 7.22 µmol of type I collagen (c-136157, Santa Cruz Biotechnology, Inc., USA), and 2 µmol of type VI collagen (ab7538, Abcam, UK). The mixture was stirred for 1 h until achieving a homogeneous solution. In the second step, the hydrazide cross-linker (ADH, TCI Europe, Belgium) was dissolved in deionised water at the concentration of 18 g/L and incorporated into the solution, while the pH was adjusted to 4.75 using 1 M HCl (Fisher Scientific, France). The carbodiimide reagent (EDCI, TCI Europe, Belgium) was dissolved in deionised water, introduced into the reaction mixture, and allowed to gel for 2 h under gentle agitation. The resulting hydrogels were then dialysed against deionised water to remove unreacted ADH and EDCI. The purified hydrogel was cast in 96-well plates, frozen, and subsequently lyophilised for 24 h using a freeze dryer (Crios, Cryotec, France; performance: 3 kg ice/24 h, T = 55 °C). Finally, the hydrogel-loaded plates were sterilised through ultraviolet (UV) irradiation over the course of 30 min.

Rheological measurements

Rheological measurements were performed using Discovery HR10 from TA Instruments (New Castle, USA), using a Peltier plane and a 25-mm plane geometry, sustained at 37 °C. The scaffold was subjected to shear stress with an oscillation measurement in a logarithmic amplitude sweep from 1 to 500 Pa at a frequency of 1 Hz. Optimal gap between the plates for the samples used in this study was found to be 100 µm. Shear modulus ($G*$) was determined as the square root of the sum of squares of the shear storage and loss moduli recorded in the linear viscoelastic region (LVR). The loss factor was obtained by taking the ratio of loss modulus to storage modulus. Young's modulus (E) was derived using the shear modulus and Poisson's ratio of 0.5 for hydrogels [24], using the following equation.

$$E = 2(1 + 0.5)G*$$

Stress-relaxation assays

For stress-relaxation experiment, two batches of 6-well plate-shaped samples were prepared in two separate syntheses, as mentioned above. One plate each of batch 1 and batch 2 were evaluated on the day 1 after synthesis. A separate plate of batch 2 was stored at 4 °C and used on the day 30 after synthesis.

The experiment was carried out with the use of TA.XTplusC Texture Analyser (Stable Micro Systems, UK). A spherical probe of 6 mm diameter was utilised in conjunction with a 5-g load cell. The experiment involved a close to instantaneous application of mechanical stress with a solid probe onto the biomaterial fixed between two parallel plates, sustained for 60 s and released after, during which the reaction force exerted by the biomaterial onto the probe was measured.

The time-series data was analysed by a home-made Python program that used Statsmodels, SciPy, and scikit-learn libraries for model fitting and assessment [25–27] as well as Pandas, NumPy, and Matplotlib libraries for data processing and visualisation [28–30]. The signal was filtered using lowess smoothing and then used to fit a two-exponent model using nonlinear least squares curve fitting. The goodness of the fit was assessed by R^2 value and mean square error of the residuals. The models were then normalised around the maximum value.

Raman spectroscopy

Raman spectra of the scaffold and its constituents—HA, RGDS, and collagen types I and VI—were recorded in the range of 380–3800 cm^{-1} with HR Evolution spectroscope by Horiba Scientific (Horiba, Japan). HA and RGDS were examined in powder form, while collagen samples were produced by freeze-drying 2 mL of collagen I and VI at -50 °C for 24 h. Scaffold samples were prepared as described above. For HA, RGDS, and collagen type I, a 632.8-nm laser was used as an excitation source with a 100 × objective lens focusing 15 mW at the sample in air interface at ambient conditions, resulting in an approximately 1 μm^2 laser spot. The spectrometer was equipped with diffraction grating of 300 grooves/mm which gave rise to the spatial resolution of 2 wavenumber per pixel. Prior to data collection, the instrument was calibrated with Raman line of silicon at 520.7 cm^{-1}. During the recording, single spectral acquisitions of 120 s duration were performed for each sample. Collagen type VI spectra were collected using 785-nm laser with double spectral acquisitions, 100 s long. Data processing was performed in LabSpec 5 software (Horiba Jobyn Yvon). An 8-degree polynomial baseline correction was applied to remove any fluorescence noise. Average spectra were produced for three specimens of each chemical.

Scanning *electron* microscopy

Scaffolds were imaged with a scanning electron microscope (SEM) ULTRA 55 (Carl Zeiss Microscopy GmbH, Germany) at 10 keV, working distance around 12 mm. Pores were measured using ImageJ software. Pore identification was achieved by applying 'Band Pass Filter' smoothing tool followed by pixel intensity histogram thresholding with 'Li Thresholding' tool [31] to separate the foreground, represented by fibres, and background, represented by pores. After this, the resulting binary image was quantified using the 'Analyze Particles' tool. The porosity was assessed by taking the ratio of cumulative area of all openings against the total observed area of the SEM image, given as a percentage.

Cell culture, glucose-stimulated insulin secretion, and insulin quantification

MIN6 cells (RRID:CVCL_0431, AddexBio, USA) were cultivated in complete MIN6 medium, which comprised DMEM medium with a glucose concentration of 4.5 g/L (31,966–021, Gibco, USA). The medium was supplemented with 15% foetal bovine serum, 100 µg/ml penicillin–streptomycin, and 55 µM β-mercaptoethanol (M6250, Sigma-Aldrich, USA). The cells were cultured at a temperature of 37 °C with a CO_2 concentration of 5%. At the day 0 of the experiment, the cells were detached from a T75 flask with trypsin and seeded on a 96-well plate (353,072, Corning, USA) in the concentration 100×10^3 cells/well. For the 3D condition, the 96-well plates contained the matrix in each well. The plates were incubated in the same conditions, as described above for 7 days.

Media changes took place every 2 days. Glucose-stimulated insulin secretion (GSIS) was performed on the days 3 and 7 of culture. MIN6 cells underwent a 1-h starvation period using Krebs–Ringer bicarbonate buffer (KRB) supplemented with 0.5% Bovine Serum Albumin (BSA, A7030, Sigma-Aldrich, USA) and 2.8 mM glucose (G8769, Sigma-Aldrich, USA). Subsequently, cells were treated with 2.8 mM glucose KRB for 1 h, followed by 20 mM glucose KRB treatment for 1 h. Insulin content was determined after cell lysis with 180 mM HCl and 75% ethanol, followed by neutralisation with 1 M Na_2CO_3. After each treatment stage and lysis, supernatant was sampled from the wells to a sampling plate. Secreted and content insulin concentrations were evaluated using enzyme-linked immunosorbent assay (ELISA, mouse ELISA insulin kit, Mercodia). Results were expressed as a percentage of insulin content. The experiment was repeated twice.

Metabolic activity and viability measurements

The metabolic activity of the MIN6 cells was evaluated on the days 0, 3, and 7 with resazurin reduction assay. Resazurin sodium salt (B21187, Fisher Scientific, France) was dissolved in deionised water to make a 1 mM working solution. The solution was sterilised with a 0.22-µm syringe filter. MIN6 cells were seeded as described above. Prior to the assay, fresh media were added to each well. Next, a total of 100 µl of working solution was added to each well and samples were incubated for 4 h at 37 °C, 5% CO_2. One hundred microliters of media was collected to a sampling plate (353,072, Corning, USA), which was read with Infinite 200 PRO microplate reader (Tecan Group Ltd., Switzerland). Fluorescence signal was recorded using 550/9 nm excitation and 590/20 nm emission monochromators. A standard curve was produced and was used to determine the cell number based on the fluorescence value, arising from the overall metabolic activity of the cells in the sampled wells. For this, the assay was performed for a range of varied cell densities (0, 10, 20, 40, 100, 200, 400×10^3 cells per well) on the day 0, after complete cell attachment on the bottom of the well was observed. Cell viability was measured using MTT assay. Measurements were performed on the days 3 and 5 of culture. At each time point, 20 µL of MTT (475,989, Sigma-Aldrich, USA) solution (5 mg/mL in PBS) was added to each well of a 96-well plate containing either 2D or 3D cultures. The plate was incubated for 4 h at 37 °C, 5% CO_2 in the dark. After incubation, the supernatant was removed, and 150 µL of dimethyl sulfoxide (DMSO) was added and the plates were incubated for 20 min at room temperature. Absorbance was measured at 540 nm. Each experimental set consisted of 6 data points, including 1 control and 5 cell-cultured samples. The data was given as a percentage viability relative to the day 3.

Immunostaining and fluorescence imaging

For fluorescence imaging, after 7 days of culture, the cell-loaded scaffold wells and chamber slides (Lab-Tek™ II CC2™ Chamber Slide, 154,941, Thermo Fisher Scientific, France) were filled with a fixing solution of paraformaldehyde (4%) in PBS and kept at room temperature for 20 min. Following fixation, blocking was performed using a blocking buffer of 1% BSA. Guinea pig anti-insulin primary antibodies (IR00261-2, Agilent Technologies, USA) were then applied and incubated overnight at 4 °C. Subsequently, cells were washed with PBS and incubated with anti-guinea pig 647 nm secondary antibodies (A21450, Invitrogen, USA) for 1 h at room temperature to visualise intracellular insulin. Lastly, nuclear staining was achieved using 4′,6-diamidino-2-phenylindole (DAPI) for 15 min, followed by thorough washing with PBS. Confocal imaging was conducted using Zeiss Axio Observer Z1 inverted microscope (Carl Zeiss Microscopy GmbH, Germany) equipped with CSU-X1 spinning-disc unit (Yokogawa Electric Corporation, Japan) and a sCMOS PRIME 95B camera (Teledyne Photometrics, USA). 2D slides were imaged with 40 × objective lens. For three-dimensional scaffold samples, a z-stack was obtained containing 100–200 images focused at a range of equally spaced planes across the z-axis with a 63 × objective lens. Image processing was performed using ZEN Microscopy Software (Carl Zeiss Microscopy GmbH, Germany). A single 2D-projection image was compiled from the z-stack, based on the maximum intensity of the pixels for each x–y coordinate, thus producing a pseudo-3D image as viewed from the top. Additionally, 3D reconstruction images were obtained from the z-stacks. Control experiments excluding primary antibodies were performed to assess the specificity of staining.

RNA extraction and qRT-PCR analysis

RNA samples were extracted using TRIzol agent (15,596,026, Invitrogen, USA). Prior to extraction, hydroscaffolds were transferred into an Eppendorf tube with Trizol agent and homogenised using a 1-mL syringe fitted with a 19G needle to ensure efficient disruption of the scaffolds. After homogenisation, 200 µL of chloroform was added, and samples were vigorously shaken for 10 s, followed by incubation at room temperature for 3 min. Centrifugation was performed at 12,000 *g* for 15 min at 4 °C to separate the phases. The aqueous phase was transferred to a new tube and 500 µL of isopropanol was added to precipitate RNA. Samples were incubated at room temperature for 15 min, followed by centrifugation at 12,000 *g* for 10 min at 4 °C. The RNA pellet was washed twice with 1 mL of 75% ethanol, air dried, and resuspended in 10–20 µL of RNase-free water. mRNA expression was measured after reverse transcription

by quantitative RT-PCR (qRT-PCR) as previously described [32] with FastStart SYBR Green master mix (Roche, Switzerland) using a LC480 instrument (Roche, Switzerland). qRT-PCR results were normalised to endogenous cyclophilin reference mRNA levels. Results are expressed as the relative mRNA levels of a specific gene expression using the formula $2-\Delta Ct$. The complete list of primers is presented in Supplemental Table 1.

Statistical analysis

Data are presented as mean ± s.d. or s.e.m. Two-sided Grubbs test was systematically performed to identify outliers, using Prism 10.0 (GraphPad software). Statistical analyses were performed using a two-tailed unpaired Mann–Whitney *U* test or two-way ANOVA with Fisher's LSD tests. Differences were considered statistically significant at $p<0.05$ ($*p<0.05$, $**p<0.01$, $***p<0.001$, and $****p<0.0001$).

Results

Mechanical characterisation of the scaffold

Rheological analysis was first performed to evaluate the shear mechanical properties of the matrix. BIOMIMESYS® scaffold, transformed in its hydrogel form by adding MIN6 culture medium, was subjected to harmonically varying loading to evaluate the shear property of the material. Storage modulus (G') and the loss modulus (G'') are presented as plots against deformation (γ) in Fig. 1a. The dynamics of these moduli under oscillatory loading characterised the contribution of solid and liquid phase to the mechanical properties of the scaffold, reflected in G' and G'', respectively. Notably, the storage modulus exceeded the loss modulus, indicating that the scaffold exhibited gel-like behaviour of a viscoelastic solid. Within the range of low deformations (< 10%), both G' and G'' remained constant, indicating an undisturbed scaffold structure. This region is

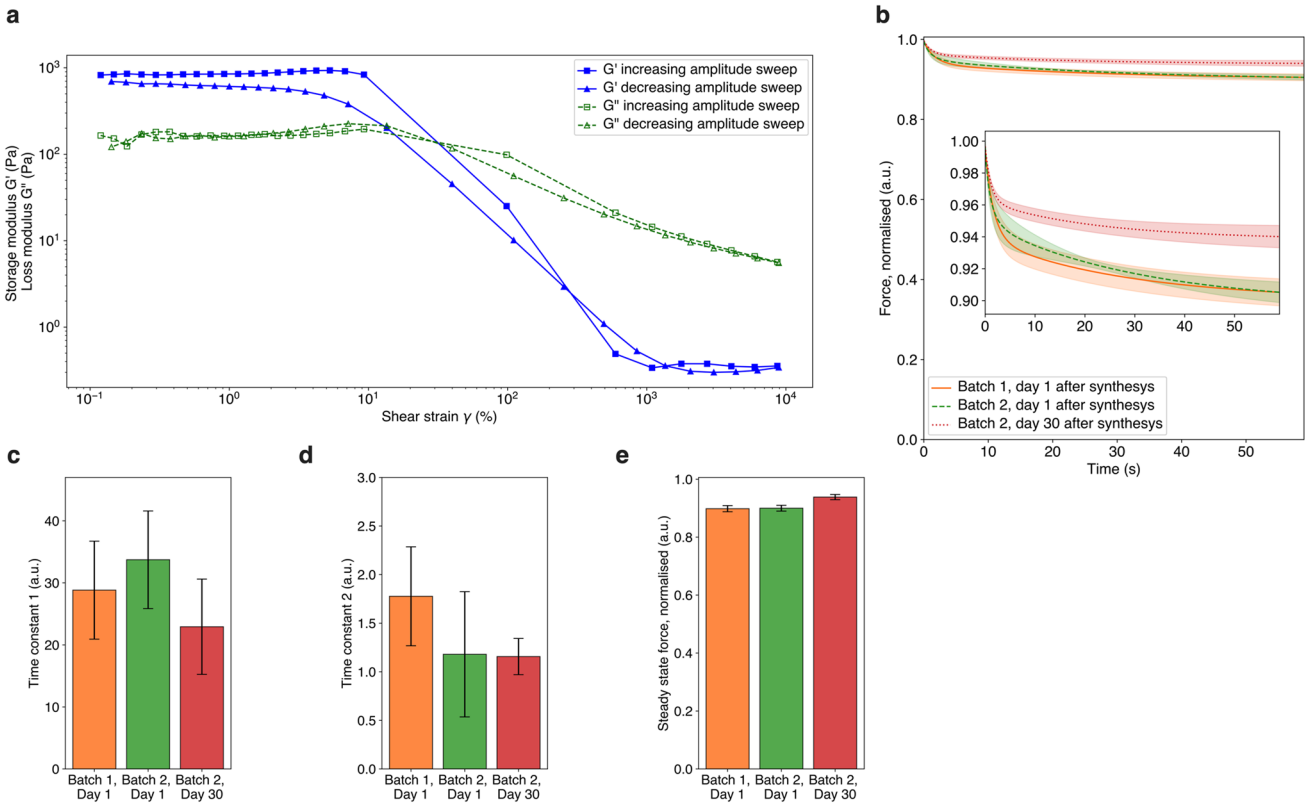

Fig. 1 Mechanical characterisation of the hydrogel scaffold. Scaffold's mechanical properties were evaluated in rheological shear oscillation test (**a**) and stress-relaxation test (**b–f**). In rheological evaluation, an oscillatory shear stress was applied from 1 to 500 Pa at a frequency of 1 Hz, 37 °C and storage (G') and loss (G'') moduli were recorded. In stress-relaxation experiment, samples were fixed between two parallel plates with an opening and subjected to a constant loading applied for 60 s through a spherical probe (**b**). The stress-relaxation curves were filtered and fitted a 2-exponent Maxwell model, normalised against the maximum value. Averages and standard deviations of the curves for batch 1 ($n=6$) and batch 2 ($n=4$) on the 1st day after synthesis and batch 2 1 month after synthesis ($n=6$) are presented in **c**. Two time constants and steady-state force were extracted from the 2-exponent model parameters and compared in **c**, **d**, and **e**, respectively

called linear viscoelastic region (LVR). Consequently, the moduli began to decrease, signifying structural perturbation. The backward sweep curves (i.e. decreasing deformation) demonstrated the reversibility of the scaffold's structure, characterised by a return close to the original values of G' and G''. The plateau values observed for G' and G'' within the LVR related to the scaffold's mechanical properties, such as rigidity or elasticity. The shear modulus G^* was found to be 815.37 ± 165.08 Pa and the average loss factor $\tan(\delta) = 0.187$. Young's modulus E, or elastic modulus, was calculated using Poisson's equation, producing the value of 2446.1 ± 495.23 Pa.

During the stress-relaxation experiment, the scaffold was subjected to a constant loading by applying a fixed deformation and sustaining it for 60 s, while the stress was recorded. The setup is shown in Supplemental Fig. 1. The response of the material was a dynamic nonlinear relaxation to a steady state from an initial value. A transient response was observed with an initial steep negative gradient converging to zero over time. This provided further insight into the viscoelastic characteristic of the complex material. A generalised Maxwell model [33] was used in order to describe the behaviour of the scaffold with spring-dashpot elements connected in parallel (details are provided in Supplemental Fig. 2). Springs represent the elastic property of the scaffold while dashpots viscous. It was found that the second-order model with two parallel elements was sufficient to represent the observed relaxation response:

$$\sigma(t) = \sigma + \left(\frac{\eta_1}{E_1} + \frac{\eta_2}{E_2}\right)\frac{d\sigma}{dt} + \frac{\eta_1\eta_2}{E_1E_2}\frac{d^2\sigma}{dt^2} \quad (1)$$

where σ is the stress, η_1 and η_2 are the viscosity coefficients of the corresponding dashpot element, and E_1 and E_2 are the corresponding spring coefficients. An exponential solution to this model consisted of two exponential elements and was expressed as:

$$F(t) = Ce^{\frac{-t}{T_1}} + \left(F(t=0) - C - F_{ss}\right)e^{\frac{-t}{T_2}} + F_{ss} \quad (2)$$

where $F(t=0)$ is the initial reaction force, F_{ss} is the steady state force and C is the parametric coefficient, and T_1 and T_2 are the time constants, describing the speed of relaxation of the biomaterial. These time constants were related to the differential form parameters as the ratio η/E. The experimental data was fit to the model (2) and the average fits are presented in Fig. 1b. The model parameters were shown to be repeatable between samples, giving aggressive $T_1 = 36.43 \pm 3.10$ and a steadier $T_2 = 1.49 \pm 0.36$, with the reaction force converging to $F_{ss} = 0.8850 \pm 0.0076$ (normalised against the initial force). This behaviour was also shown to be consistent between batches and repeatable after 1 month of storage at 4 °C, as presented in Fig. 1c, d, and e.

Physico-chemical characterisation of the scaffold

Raman spectroscopy was performed on the scaffold and the major chemicals in its composition: HA, collagen types I and VI, and RGDS. The average spectra of three specimens each are presented in Fig. 2. Collagen type VI spectrum is given in the range of 380–2800 cm^{-1}, due to poor sensitivity of the sensor at higher wavenumber for the laser configuration used. The spectral patterns of both collagen types appeared alike, since they were similar in their chemical composition. The presence of the amide bands was observed in the spectra of HA, RGDS, collagens, and the scaffold. For instance, amide I band is observed in 1630–1690 cm^{-1} region, arising from the C = O stretching vibration. While it occurs at higher wavenumber for HA, RGDS, and collagen samples, the peak is downshifted to 1640 cm^{-1} in the scaffold suggesting a conformational change from β-sheet to α-helix [34]. As well as this, amide III peaks at 1238 cm^{-1} and 1266 cm^{-1} are observed in all spectra, arising from C-N stretching and N–H bending. N–H in-plane deformations were also observed in the scaffold spectrum at 1426 cm^{-1}, the same as in collagens' and RGDS spectra. The peaks in the 890 cm^{-1} and 938 cm^{-1} bands appear in the scaffold spectrum and relate to breathing of proline ring and C–C stretching of collagen and RGDS backbone, respectively. At the same time, together with the 1125 cm^{-1} peak, they can also be associated with stretching of C–O–C glycosidic bond, forming the polysaccharide backbone of the HA. Furthermore, the 1049 cm^{-1} peak is both manifested in HA and as a shoulder on the scaffold spectrum, assigned to C-O stretching vibration of the alcoholic group (-OH). Similar vibrations are inherited by the scaffold from RGDS, visible at 1078 cm^{-1}. The 1374 cm^{-1} peak arising from C-H and CH_2 out of plane deformations can be observed in both HA and scaffold's spectra, as well as the CH stretching peak at 2907 cm^{-1}. In addition to this, the scaffold inherits the CH_3 and CH_2 deformation peaks at 1450 cm^{-1} and 2937 cm^{-1} regions from collagen. A pronounced peak at 1156 cm^{-1} corresponding to C-N stretching signifies new cross-links formed between the carbonyl and amine groups of HA and collagen. A notable peak in 1296 cm^{-1} in the scaffold's spectrum has resulted from the CH_2 methylene twisting of the cross-linking agent ADH. As well as this, a group of high-intensity peaks in 3150–3350 cm^{-1} wavenumber region in the spectrum of the scaffold can be associated with N–H stretching arising from EDCI/NHS urea linkages formed between the polysaccharide chains during the synthesis [35–37].

Physical structure of cell-free scaffolds was then examined under the SEM (Fig. 3a). The biomaterial can be characterised as a mesh of interlinked thin non-uniform irregular concave-shaped structures of varied sizes, arising from the

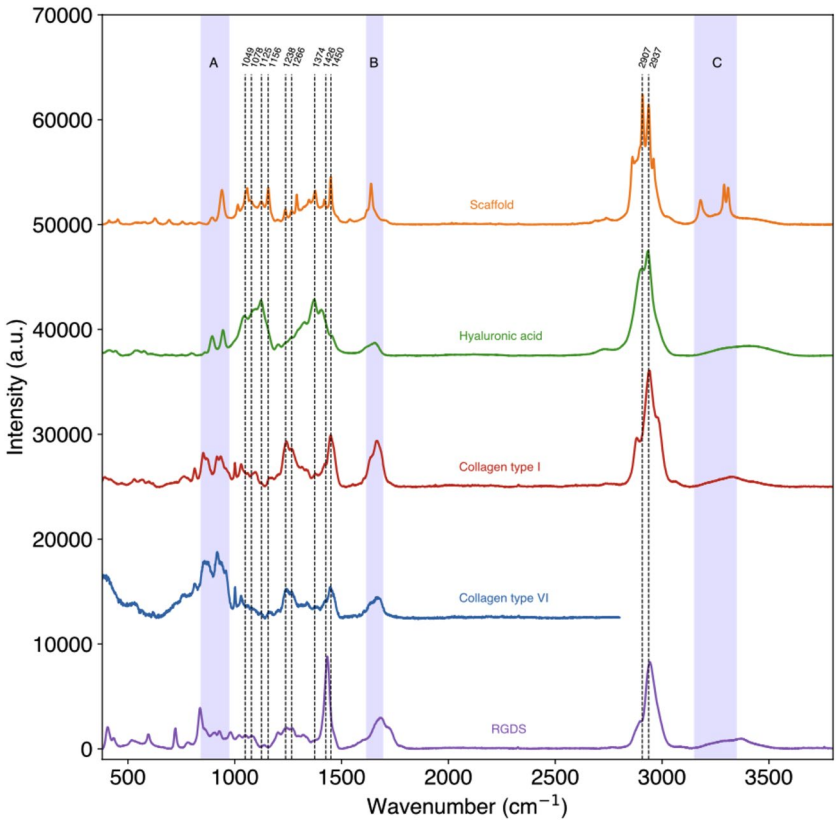

Fig. 2 Chemical characterisation of scaffold and its constituents. Raman spectroscopy curves of scaffold (yellow), hyaluronic acid (green), collagen type I (red), collagen type VI (blue), and RGDS (purple). The highlighted regions are C–C and C–O–C stretching bands (A), amide I band (B), and N–H stretching bands (C). Three samples were prepared for each material and spectra were collected in dry conditions at ambient temperature. Fluorescence noise was removed with polynomial baseline correction and average curve for each chemical is presented ($n=3$). For collagen type VI, a longer wavelength laser was used to avoid autofluorescence. Hence, only 380–2800 cm^{-1} range is presented due to limited sensitivity of the spectrometer in this laser configuration

cross-linked HA-collagen fibres. A homogeneous network of highly open and interconnected pores formed between the fibres. The pores appear evenly distributed across the entire volume of the scaffold, as evident from top (Fig. 3b), cross-section (Fig. 3c), and bottom (Fig. 3d) images. The average porosity was determined as $47.76 \pm 4.48\%$ with pore diameter ranging from 1.82 to 135.07 µm, providing enough volume for structural support of biological cells. The scaffold was thus demonstrated to exhibit both the expected chemical and structural composition.

MIN6 proliferation, viability, gene expression, and insulin secretion in 2D versus 3D culture

MIN6 cell line was used to assess the functionality of the scaffold as a 3D pancreatic in vitro model in the context of cell proliferation and insulin secretion in response to glucose stimulation. The proliferation and viability of MIN6 cells was evaluated during 5 to 7 days of incubation and assessed by measuring metabolic activity using resazurin and MTT assays, respectively, as shown in Fig. 4a and b. The growth rates followed a similar pattern for both two- and three-dimensional cultures. There was a rapid increase in metabolic activity at the day 3, compared to the day 0, followed by a more gradual growth until day 7. Nonetheless, the proliferation rate at both days 3 and 7 appeared faster in the 3D culture compared to 2D culture. Scaffold-seeded cells reached 400% by the day 3 and 550% by the day 7, compared to the steadier 260% and 320% proliferation in the classic culture on the corresponding days, relative to the day 0 metabolic activity. This can be accounted for by the observation that confluence is reached in the 2D condition. In MTT assays, we observed that cells in 2D had the same viability at day 3 and day 5 in 2D (Fig. 4b). However, viability of MIN6 cells was much more improved at day 5 compared to day 3 in 3D, suggesting that 3D culture could improve viability of MIN6 cells with time.

After 7 days of culture, MIN6 cells cultured on the classic plastic 2D surface reached confluence, spreading flat over the entire available surface (Fig. 4c). On the other hand, z-stack immunofluorescent imaging of the 3D culture, presented in Fig. 4d, e, and f, revealed the organisation of MIN6 cells into clustered spheroid structures that express insulin at the protein level. The clusters of 20–40 cells were observed to have been scattered across the entire volume of the scaffold. The shape of the clusters was rather asymmetrical in x- and y-directions and oblate in z-direction, with width ranging from 40 to 120 µm and thickness from 20 to 40 µm. These observations suggested that the cells have migrated, adhered, and divided within the pores

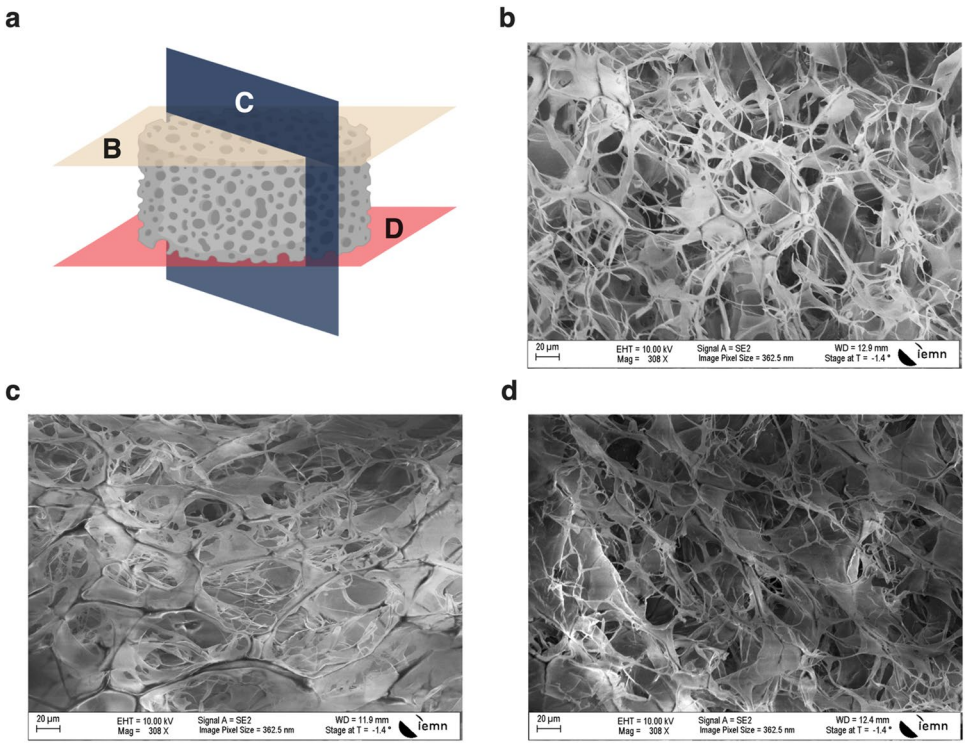

Fig. 3 Surface characterisation of the hydrogel scaffold. SEM images, as explained on the schematic **a,** showing the microstructure of the top (**b**), section (**c**), and bottom (**d**) of the scaffold. The scaffolds were freeze dried prior to imaging. No sputter coating was required, as fibres were detectable at 10 kV with minimal charging effect. Porosity of the scaffold was assessed by observing the open areas between the fibres

of the scaffold, self-distributing over the available space in 3D during the 7-day culture. To evaluate whether 2D or 3D culture could modify gene expression, we assessed mRNA expression levels of key β-cell identity genes (*Ins1*, *Ins2*, *Slc2a2*, *Pcsk1*, *Glp1r*, *Ucn3*, *Pdx1*, *Mafa*, *Nkx6.1*) and other pancreatic islet genes (*Gcg*, *Sst*) through qRT-PCR. Although most of the gene expression were found similar in MIN6 cells cultivated in 2D and 3D for 3 and 7 days, we observed that the expression of the transcription factor *Nkx6.1*, a key gene involved in insulin secretion and β-cell identity, was increased in 3D condition at day 3 compared to 2D (Fig. 4g). These data suggest that 2D or 3D cultures may have biological effects in modifying the transcriptome of MIN6 cells.

The regulation of insulin secretion by the MIN6 cells in response to variation of glucose concentration in GSIS experiment was then measured as presented in Supplemental Fig. 3 and Fig. 5. The increase of secreted insulin in 20 mM glucose conditions was maintained for both conditions on the days 3 and 7 (Fig. 5a and b, respectively). Despite the increased cell number, insulin content was not significantly different in MIN6 cells maintained in 2D or 3D at day 3 (Fig. 5b) and day 7 (Fig. 5d). When normalised against total insulin content, the percentage of secreted insulin was maintained after 7 days of culture in 2D, although the amplitude of the response was decreased. In the 3D condition, MIN6 cells were still responding to a 20 mM glucose stimulation, yet again the response was diminished compared to day 3. Overall, the data suggest that the secretory activity of MIN6 was analogous for 2D and 3D cultures in short-term conditions, confirming the maintained functionality of the cells seeded on the scaffold.

Discussion

The results presented in this study demonstrate the successful synthesis of a biomimetic scaffold that mimics the pancreatic ECM for application with a 3D cell culture of MIN6 cells. The scaffold's viscoelastic properties, porous structure, and incorporation of key ECM components provide a more physiologically relevant environment for cell growth and function compared to traditional 2D culture systems.

Current literature lacks sufficient data on the mechanical properties of pancreatic tissue. The elastography approaches have previously demonstrated shear stiffness of human pancreas to range from 0.72 to 1.54 kPa at 40 Hz [38, 39], whereas Wex et al. reported 0.64 to 1.17 kPa in rheological experiments with tan(δ) between 0.3 and 0.4 [40]. Therefore, the shear stress attributes of the synthesised ECM scaffolds are comparable with the existing data on the pancreatic tissue.

The production and storage of the scaffold are demonstrated here to have little to no effect on the response to loading, thus confirming the reproducibility of the fabrication method. The double-exponent stress-relaxation model

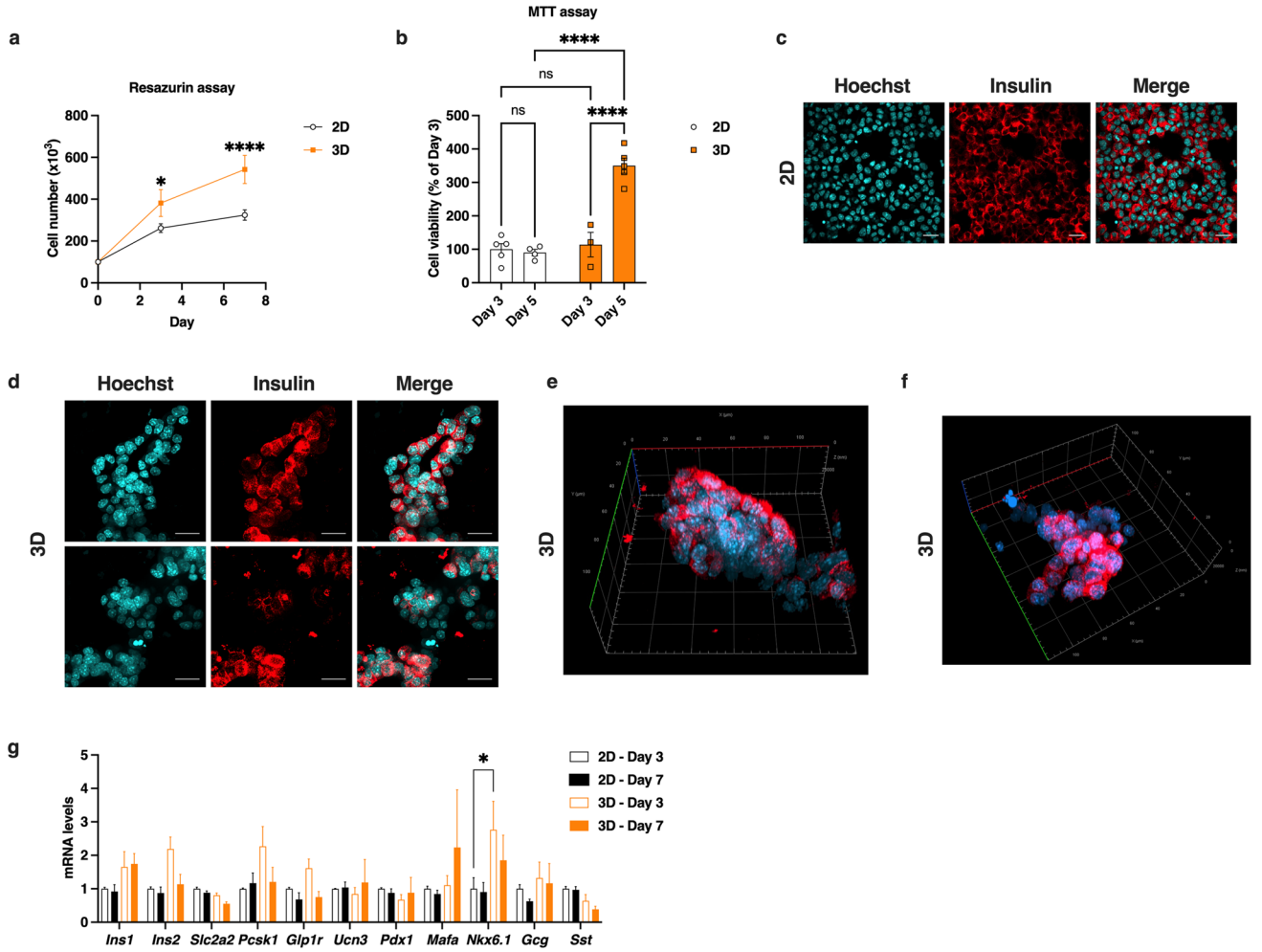

Fig. 4 MIN6 proliferation, viability, confocal imaging, and gene expression analysis of MIN6 cells in 2D and 3D culture. **a** MIN6 cells were cultivated on classic 2D plastic surface and in 3D culture on scaffolds in 96-well plates for 7 days at the concentration 10^{-5} cells/well. Proliferation was assessed with resazurin assay performed on days 3 and 7. Standard curve was produced to relate the fluorescence to cell number by assessing the activity of cells seeded at various concentrations and resazurin assay taken on day 0 after cell sedimentation. Obtained cell number data is presented as averages with standard deviations in **a** ($n=3$). **b** Viability assays using MTT was performed on day 3 and day 7 of MIN6 cells cultured in 2D and 3D. Data are presented as percentage over 2D at day 3 ($n=3$–5). **c**–**f**) Immunofluorescence confocal images of MIN6 cells demonstrate high level of confluence in 2D and cluster formation in 3D after 7 days of culture. Cells were fixed and stained for nuclei (cyan) and insulin (red). The images of 2D samples were obtained from a single focal plane (**c**). Scale bar = 20 µm. For 3D samples, confocal spin disc microscope was used to take a stack of images at 100–200 focal planes in z-direction, separated by 0.2 µm. **d** Maximum intensity projection image of z-stack, depicting an example of β-cell cluster. Scale bar = 20 µm. **e**–**f** 3D reconstructions of z-stack confocal fluorescent images showing two MIN6 spheroids in the spatial domain. **g** mRNA expression levels of key β-cell identity genes (*Ins1*, *Ins2*, *Slc2a2*, *Pcsk1*, *Glp1r*, *Ucn3*, *Pdx1*, *Mafa*, *Nkx6.1*) and other pancreatic islet genes (*Gcg*, *Sst*) in MIN6 cells cultivated in 2D and 3D for 3 and 7 days. Results in **a**, **b,** and **g** are displayed as means ± SEM. *$p<0.05$, ****$p<0.0001$. *ns*, not significant

presented here highlights the complexity of the time-dependent viscoelastic behaviour of the material. Thus, the dynamics between the two time constants, where T_2 is significantly less than T_1 and steady state at 88.5% of the initial force, suggest pronounced elastic characteristics. The latter implies strong dominance of the solid phase of the material, in line with the rheological observations. Conversely, a single exponent model has been found to be a better fit for the experimental results of human pancreas viscous relaxation in the study of Rubiano et al. [41]. As well as this, the relaxation to lower steady-state force is often observed over a longer time frame [42]. Thus, despite shear properties closely resembling those of pancreas, the time-transient dynamic of the scaffold falls short of the biological tissue. That said, the available literature on the mechanical properties of pancreatic tissue is scarce and this topic could be further explored.

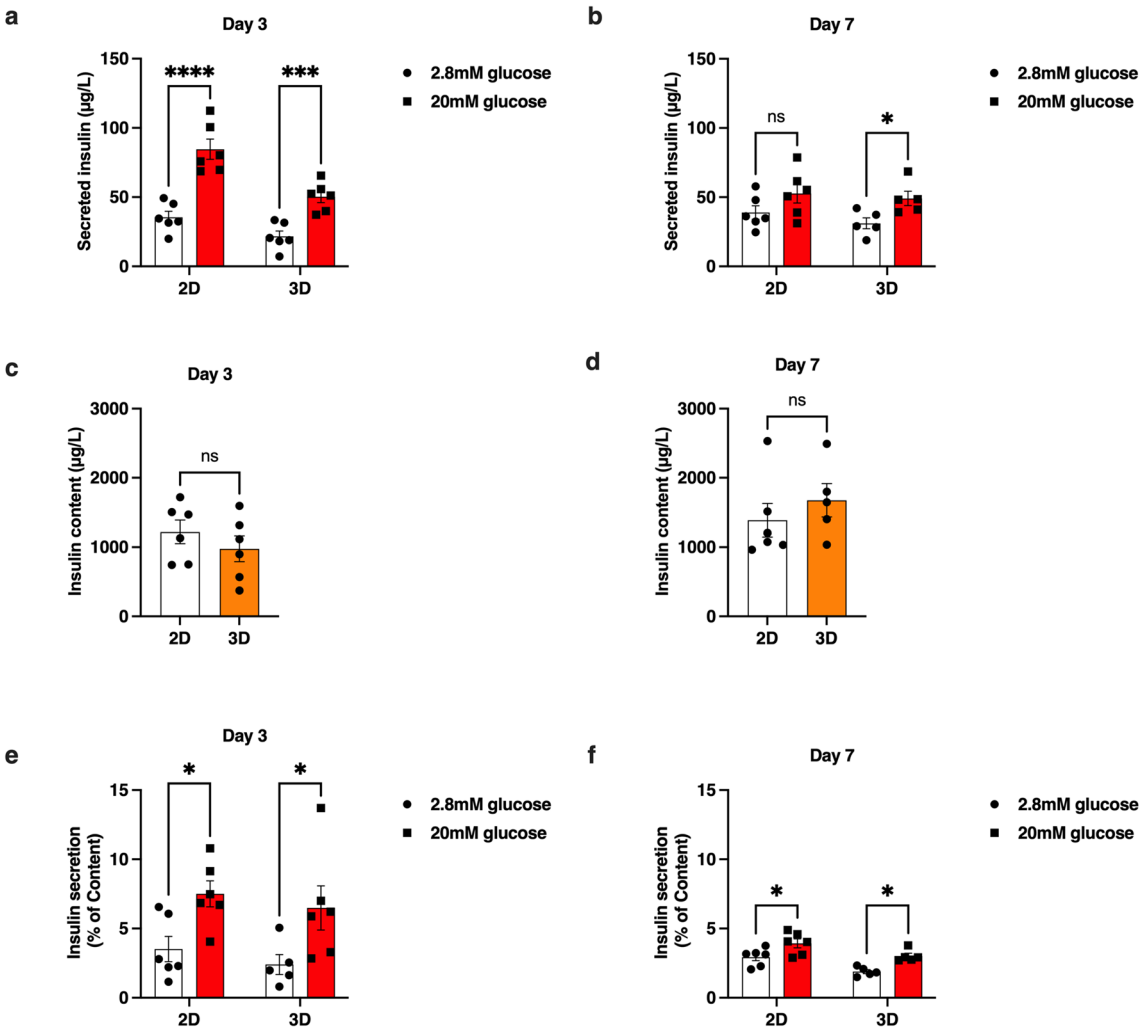

Fig. 5 Insulin secretion in response to glucose in 2D and 3D cultivated-MIN6 cells. GSIS assay was performed on days 3 and 7. Secreted insulin concentration values after stimulation with 2.8 and 20 mM glucose (**a–b**) were normalised against total insulin content (**c–d**) in each well and given as percentage of content (**e–f**). Average and standard deviation values of insulin secretion and content are presented ($n = 6$). *$p < 0.05$, ***$p < 0.001$, and ****$p < 0.0001$

Raman spectroscopy confirmed the presence of key ECM components in the scaffold. The appearance of amide bands, indicative of peptide bonds, as well as correlation of specific vibrations suggests successful incorporation and cross-linking of HA and type I collagen through amide chemistry. Furthermore, the observed conformational changes of these components within the scaffold may have implications for cell attachment and growth, presenting niches for integrin binding. As well as this, urea cross-links formed between the polysaccharide chains enhance the stability and structural integrity of the scaffold. These findings are consistent with previous studies that have demonstrated the importance of ECM composition in regulating cell behaviour and function [43, 44].

Our metabolic activity experiments involving MIN6 cells demonstrate an initial adaptation phase followed by a more gradual growth phase. During the latter stage, the spatial capacity provided by the pores within the scaffold allows cells to continue proliferating without reaching confluence as quickly as in the 2D culture. This is achieved as a result of the scaffold mimicking the native extracellular matrix more closely and providing a favourable microenvironment for cell growth and survival [45].

'Pseudoislet' generation methods with MIN6 cells have been previously employed to improve the insulin secreting function compared to simple monolayer cultures thanks to increased cell-to-cell contact [46–49]. Using our ECM-mimicking scaffold, we demonstrate the formation of multiple

MIN6 spheroids in 3D, closer resembling the islets of Langerhans in native tissue. We have shown that MIN6 insulin secretion functionality was maintained over the course of 1 week culture in 3D, consistent with classic culture. Despite the higher proliferation rate and viability in 3D compared to the 2D culture, the total insulin content values, *Ins1* and *Ins2* gene expression were similar in both conditions. Klochendler et al. had reported that cell cycle progression in β-cells, isolated from a transgenic mouse model (Ins-rtTA; TET-DTA), was associated with reduced expression of β-cell-specific genes [50]. Similarly, it has been shown by Puri et al. that INS-1 cell line had deregulated insulin secretion and production linked genes and showed diminished GSIS as the cells were entering the cell cycle [51]. In addition to this, the studies on human β-cell lines EndoC-βH reported that GSIS efficiency could be improved by removing proliferating properties [52]. Such phenomenon could be explained by partial β-cell de-differentiation observed during high proliferative activity, since both processes (i.e. insulin production and cell proliferation) have high energy demand and require to shut down one or the other. In our model, both processes are operating at the same time, suggesting that in 3D, MIN6 cells are capable of maintaining β-cell identity gene levels while proliferating. Further studies are required to better understand this observation.

β-cell survival, differentiation, and metabolism have been linked to mechanotransduction mechanisms acting on cell nuclei and mitochondria [53, 54]. Furthermore, MIN6 cells have been shown before to have an increased glucose sensitivity when exposed to lower stiffness biomaterials as opposed to the plastic surface of classic culture. Thus, Nyitray et al. have reported improved response to glucose stimulation in cells cultured on 0.1 kPa scaffolds, by accessing β-catenin signalling pathways [55]. On the other hand, Zhang et al. demonstrated increased insulin production and comparable secretion, utilising hydrogels as stiff as 40 and 70 kPa [56]. By targeting the mechanical properties of native tissue, we aimed to achieve a significant improvement of function; however, this was not observed. Pseudoislet size has also been reported to affect the insulin secreting capabilities of β-cells. For instance, Mendelsohn et al. have found that increasing the size of 832/13 insulinoma cell clusters from 40 to 60 and 120 μm had resulted in a dramatic rise of insulin index [57]. In our study, smaller spheroids were more prevalent, which could negatively impact the contrast in insulin secretion between low and high glucose conditions. We hypothesise that further fine-tuning the mechanical properties and pore size of our scaffold as well as longer incubation period of MIN6 could positively affect cell survival and maturation, at the same time producing larger clusters and developing higher number of cell-to-cell contacts, which in turn could further improve the insulin secreting function during high glucose exposure.

While the current study demonstrates the potential of the synthesised biomimetic scaffold in improving in vitro models of pancreatic islets, there are several limitations and future directions to consider. First, the use of MIN6 cells, while providing a convenient and well-established model as well as decreasing animal experimentation to satisfy the 3Rs initiative (Reduce, Replace, Refine) [58], may not fully recapitulate the behaviour of primary human islets [22]. MIN6 cell line was the most reliable model on our hands, which allowed high experimental throughput thanks to its lower maintenance requirements, compared to other cell lines, such as INS 823/13 or EndoC-BH1. Nonetheless, the immortalised properties and the mouse origin of MIN6 have diminished the translational relevance to human pancreas biology. At the same time, primary human islets availability is highly limited worldwide [59, 60]. Future studies should validate these findings using primary human islets or induced pluripotent stem cells (iPSC)-derived β-cells to improve the scaffold's relevance to human biology. iPSC strategies have already demonstrated their potential to be utilised in 3D models of pancreas [17, 61, 62].

Second, the long-term effects of the scaffold on cell viability, function, and differentiation should be investigated. While the current study demonstrates promising results over a 7-day period, longer-term experiments are necessary to evaluate the scaffold's ability to maintain cell function and phenotype over extended periods [18].

Third, the mechanical properties of the scaffold, such as stiffness and stress-relaxation rate, may require further optimisation to more closely mimic the native pancreatic ECM. The incorporation of additional ECM components, such as laminin [14] and heparan sulphate [63], or the modulation of cross-linking density could be explored to fine-tune the scaffold's properties and enhance its biological relevance.

Finally, further in vitro studies are necessary to assess the scaffold's performance in a more complex environment. Thanks to its high porosity, the scaffold has a potential to be utilised in a microfluidic organ-on-chip setting with dynamic fluid supply applied across the seeded matrix. Such application has already been demonstrated with a similarly synthesised matrix, mimicking the ECM of liver [64]. Additionally, vascularisation strategies or co-culture experiments with immune cells or adipose tissue could be explored in such setting as an improved model for the tissue function and/or to better understand T1D and T2D physiopathology.

Conclusion

The synthesised biomimetic scaffold presented in this study represents a promising platform for improving in vitro models of pancreatic islet studies and β-cell function. Interestingly, the scaffold's viscoelastic properties, porous structure,

and incorporation of key ECM components provide a more physiologically relevant environment for MIN6 cell growth and function. The enhanced proliferation and formation of islet-like structures in the scaffold highlight its potential for advancing the understanding of islet biology and facilitating the development of novel cell-based therapies for diabetes. Our findings suggest that the relationship between scaffold properties and cell behaviour is more complex than initially anticipated, highlighting the need for further optimisation of the scaffold design. Future studies should focus on the optimisation of scaffold properties and validation of these findings using human cells to fully realise its potential for drug screening or diagnostic applications.

Supplementary Information The online version contains supplementary material available at https://doi.org/10.1007/s44164-024-00078-z.

Acknowledgements The authors thank US 41—UMS 2014—PLBS for confocal imaging facilities and UMET CNRS UMR 8207, especially Cédric Zobrist, for assisting with rheological experiments. The authors would like to thank Mrs. Myriam Moreau for her help in carrying out the work on the micro Raman system facility of the Advanced Characterization Platform of the Chevreul Institute. The Chevreul Institute is thanked for supporting CPER projects funded by the 'Ministère de l'Enseignement Supérieur et de la Recherche', the region 'Hauts-de-France', the ERDF program of the European Union, and the 'Métropole Européenne de Lille'. We thank Laure Rolland and Vaihere Cheung for excellent technical guidance with cell culture. We also thank Emilie Courty, Véronique de Conto, Zied Sougir, Cécile Legallais, Yannick Coffinier, and members of INSERM UMR1167 and IEMN UMR8520 for their contributions in scientific discussions.

Author contribution Conceptualisation, J.S.A. and A.T.; methodology, L.P., M.R., A.M.V., Y.K., J.S.A., and A.T; investigation, L.P., N.L., M.R., A.M.V., Y.K., J.S.A., and A.T; resources, E.V., N.M., Y.K., and R.A.T.; data curation, L.P., N.L., M.R., A.M.V., A.T., and J.S.A.; writing—original draft, L.P.; writing—review and editing, A.T. and J.S.A.; visualisation, L.P.; supervision, A.T. and J.S.A.; funding acquisition, A.T. and J.S.A.

Funding This project has received funding from the European Union's Horizon 2020 research and innovation program under the Marie Skłodowska-Curie grant agreement no 847568, from the French government through the Programme Investissement d'Avenir (I-SITE ULNE/ANR-16-IDEX-0004 ULNE) managed by the Agence Nationale de la Recherche (ANR). This work was supported by the ANR grants (ANR EpiRNA-T2D ANR-23-CE14-0040), INSERM, Université de Lille, Institut Pasteur de Lille, Fondation pour la Recherche Médicale (EQU202103012732).

Data and code availability All original data and code reported in this paper will be shared by the lead contact upon request. Any additional information required to reanalyse the data reported in this paper is available from the lead contact upon request.

Materials availability All unique/stable reagents generated in this study are available from the lead contact with a completed Materials Transfer Agreement.

Declarations

Competing interests M.R., A.M.V., E.V., and N.M. are board members and/or employees of HCS Pharma, which provided BIOMIMESYS® scaffold. N.M. owns stocks in HCS Pharma. The other authors have no relevant financial or non-financial interests to disclose.

References

1. American Diabetes Association. Diagnosis and classification of diabetes mellitus. Diabetes Care. 2014;37 (Supplement_1). https://doi.org/10.2337/dc14-S081
2. Shapiro AJ, Pokrywczynska M, Ricordi C. Clinical pancreatic islet transplantation. Nat Rev Endocrinol. 2017. https://doi.org/10.1038/nrendo.2016.178.
3. Kang D, Kim J, Jang J. Advancements in biomaterials and biofabrication for enhancing islet transplantation. Int J Bioprinting. 2023. https://doi.org/10.18063/ijb.v9i6.1024
4. Weir GC, Bonner-Weir S. Islet β cell mass in diabetes and how it relates to function, birth, and death. Ann N Y Acad Sci. 2013. https://doi.org/10.1111/nyas.2013.1281.issue-1.
5. Frantz C, Stewart KM, Weaver VM. The extracellular matrix at a glance. J Cell Sci. 2010. https://doi.org/10.1242/jcs.023820.
6. Vining KH, Mooney DJ. Mechanical forces direct stem cell behaviour in development and regeneration. Nat Rev Mol Cell Biol. 2017. https://doi.org/10.1038/nrm.2017.108.
7. Chaudhuri O, Cooper-White J, Janmey PA, Mooney DJ, Shenoy VB. Effects of extracellular matrix viscoelasticity on cellular behaviour. Nat. 2020. https://doi.org/10.1038/s41586-020-2612-2.
8. Lou J, Mooney DJ. Chemical strategies to engineer hydrogels for cell culture. Nat Rev Chem. 2022. https://doi.org/10.1038/s41570-022-00364-4.
9. Wu DT, Jeffreys N, Diba M, Mooney DJ. Viscoelastic biomaterials for tissue regeneration. Tissue Eng Part C Methods. 2022. https://doi.org/10.1089/ten.TEC.2021.0386.
10. Thivolet CH, Chatelain P, Nicoloso H, Durand A, Bertrand J. Morphological and functional effects of extracellular matrix on pancreatic islet cell cultures. Exp Cell Res. 1985. https://doi.org/10.1016/0014-4827(85)90510-1.
11. Llacua LA, Faas MM, de Vos P. Extracellular matrix molecules and their potential contribution to the function of transplanted pancreatic islets. Diabetologia. 2018. https://doi.org/10.1007/s00125-018-4560-8.
12. Jiang L, Shen Y, Liu Y, Zhang L, Jiang W. Making human pancreatic islet organoids: progresses on the cell origins, biomaterials and three-dimensional technologies. Theranostics. 2022. https://doi.org/10.7150/thno.59252.
13. Guruswamy Damodaran R, Vermette P. Decellularized pancreas as a native extracellular matrix scaffold for pancreatic islet seeding and culture. J Tissue Eng Regen Med. 2018. https://doi.org/10.1002/term.2648.
14. Daoud J, Petropavlovskaia M, Rosenberg L, Tabrizian M. The effect of extracellular matrix components on the preservation of human islet function in vitro. Biomater. 2010. https://doi.org/10.1016/j.biomaterials.2009.11.050.

15. Nagata N, Gu Y, Hori H, Balamurugan AN, Touma M, Kawakami Y, Wang W, Baba TT, Satake A, Nozawa M, Tabata Y. Evaluation of insulin secretion of isolated rat islets cultured in extracellular matrix. Cell Transplant. 2001. https://doi.org/10.3727/000000001783986678.
16. Goh SK, Bertera S, Olsen P, Candiello JE, Halfter W, Uechi G, Balasubramani M, Johnson SA, Sicari BM, Kollar E, Badylak SF. Perfusion-decellularized pancreas as a natural 3D scaffold for pancreatic tissue and whole organ engineering. Biomater. 2013. https://doi.org/10.1016/j.biomaterials.2013.05.065.
17. Bi H, Karanth SS, Ye K, Stein R, Jin S. Decellularized tissue matrix enhances self-assembly of islet organoids from pluripotent stem cell differentiation. ACS Biomater Sci Eng. 2020. https://doi.org/10.1021/acsbiomaterials.0c00169.
18. Jiang K, Chaimov D, Patel SN, Liang JP, Wiggins SC, Samojlik MM, Rubiano A, Simmons CS, Stabler CL. 3-D physiomimetic extracellular matrix hydrogels provide a supportive microenvironment for rodent and human islet culture. Biomater. 2019. https://doi.org/10.1016/j.biomaterials.2018.03.023.
19. Theocharis AD, Skandalis SS, Gialeli C, Karamanos NK. Extracellular matrix structure. Adv Drug Deliv Rev. 2016. https://doi.org/10.1016/j.addr.2015.11.001.
20. Plow EF, Haas TA, Zhang L, Loftus J, Smith JW. Ligand binding to integrins. J Biol Chem. 2000. https://doi.org/10.1074/jbc.R000003200.
21. Miyazaki JI, Araki K, Yamato E, Ikegami H, Asano T, Shibasaki Y, Oka Y, Yamamura KI. Establishment of a pancreatic β cell line that retains glucose-inducible insulin secretion: special reference to expression of glucose transporter isoforms. Endocrinol. 1990. https://doi.org/10.1210/endo-127-1-126.
22. Skelin M, Rupnik M, Cencič A. Pancreatic beta cell lines and their applications in diabetes mellitus research. ALTEX. 2010. https://doi.org/10.14573/altex.2010.2.105
23. Louis F, Pannetier P, Souguir Z, Le Cerf D, Valet P, Vannier JP, Vidal G, Demange E. A biomimetic hydrogel functionalized with adipose ECM components as a microenvironment for the 3D culture of human and murine adipocytes. Biotechnol Bioeng. 2017. https://doi.org/10.1002/bit.26305.
24. Ahearne M, Yang Y, El Haj AJ, Then KY, Liu KK. Characterizing the viscoelastic properties of thin hydrogel-based constructs for tissue engineering applications. J R Soc Interface. 2005. https://doi.org/10.1098/rsif.2005.0054.
25. Seabold S, Perktold J. Statsmodels: econometric and statistical modeling with Python. SciPy. 2010. https://doi.org/10.25080/Majora-92bf1922-011
26. Virtanen P, Gommers R, Oliphant TE, Haberland M, Reddy T, Cournapeau D, Burovski E, Peterson P, Weckesser W, Bright J, Van Der Walt SJ. SciPy 1.0: fundamental algorithms for scientific computing in Python. Nat Methods. 2020. https://doi.org/10.1038/s41592-019-0686-2
27. Pedregosa F, Varoquaux G, Gramfort A, Michel V, Thirion B, Grisel O, Blondel M, Prettenhofer P, Weiss R, Dubourg V, Vanderplas J. Scikit-learn: machine learning in Python. J Mach Learn Res. 2011. https://doi.org/10.5555/1953048.2078195.
28. Harris CR, Millman KJ, Van Der Walt SJ, Gommers R, Virtanen P, Cournapeau D, Wieser E, Taylor J, Berg S, Smith NJ, Kern R. Array programming with NumPy. Nat. 2020. https://doi.org/10.1038/s41586-020-2649-2.
29. McKinney W. Data structures for statistical computing in Python. SciPy. 2010. https://doi.org/10.25080/Majora-92bf1922-00a
30. Hunter JD. Matplotlib: A 2D graphics environment. Comput Sci Eng. 2007. https://doi.org/10.1109/MCSE.2007.55.
31. Li CH, Lee CK. Minimum cross entropy thresholding. Pattern Recognit. 1993. https://doi.org/10.1016/0031-3203(93)90115-D.
32. Oger F, Bourouh C, Friano ME, Courty E, Rolland L, Gromada X, Moreno M, Carney C, Rabhi N, Durand E, Amanzougarene S. β-cell–specific E2f1 deficiency impairs glucose homeostasis, β-cell identity, and insulin secretion. Diabetes. 2023. https://doi.org/10.2337/db22-0604.
33. Efremov YM, Okajima T, Raman A. Measuring viscoelasticity of soft biological samples using atomic force microscopy. Soft Matter. 2020. https://doi.org/10.1039/C9SM02004B.
34. McColl IH, Blanch EW, Gill AC, Rhie AG, Ritchie MA, Hecht L, Nielsen K, Barron LD. A new perspective on β-sheet structures using vibrational Raman optical activity: from poly(L-lysine) to the prion protein. J Am Chem Soc. 2003. https://doi.org/10.1021/ja029310d.
35. Martinez MG, Bullock AJ, MacNeil S, Rehman IU. Characterisation of structural changes in collagen with Raman spectroscopy. Appl Spectrosc Rev. 2019. https://doi.org/10.1080/05704928.2018.1533085
36. Talari ACS, Movasaghi Z, Rehman S, Rehman IU. Raman spectroscopy of biological tissues. Appl Spectrosc Rev. 2015. https://doi.org/10.1080/05704928.2014.923902
37. Essendoubi M, Gobinet C, Reynaud R, Angiboust JF, Manfait M, Piot O. Human skin penetration of hyaluronic acid of different molecular weights as probed by Raman spectroscopy. Skin Res Technol. 2016. https://doi.org/10.1111/srt.12239.
38. Shi Y, Glaser KJ, Venkatesh SK, Ben-Abraham EI, Ehman RL. Feasibility of using 3D MR elastography to determine pancreatic stiffness in healthy volunteers. J Magn Reson Imaging. 2015. https://doi.org/10.1002/jmri.24651.
39. Shi Y, Cang L, Zhang X, Cai X, Wang X, Ji R, Wang M, Hong Y. The use of magnetic resonance elastography in differentiating autoimmune pancreatitis from pancreatic ductal adenocarcinoma: a preliminary study. Eur J Radiol. 2018. https://doi.org/10.1016/j.ejrad.2018.09.010.
40. Wex C, Fröhlich M, Brandstädter K, Bruns C, Stoll A. Experimental analysis of the mechanical behavior of the viscoelastic porcine pancreas and preliminary case study on the human pancreas. J Mech Behav Biomed Mater. 2015. https://doi.org/10.1016/j.jmbbm.2014.10.014.
41. Rubiano A, Delitto D, Han S, Gerber M, Galitz C, Trevino J, Thomas RM, Hughes SJ, Simmons CS. Viscoelastic properties of human pancreatic tumors and in vitro constructs to mimic mechanical properties. Acta Biomater. 2018. https://doi.org/10.1016/j.actbio.2017.11.051.
42. Schmuck RB, Lippens E, Wulsten D, Garske DS, Strönisch A, Pratschke J, Sauer IM, Duda GN, Bahra M, Cipitria A. Role of extracellular matrix structural components and tissue mechanics in the development of postoperative pancreatic fistula. J Biomech. 2021. https://doi.org/10.1016/j.jbiomech.2021.110714.
43. Rozario T, DeSimone DW. The extracellular matrix in development and morphogenesis: a dynamic view. Dev Biol. 2010. https://doi.org/10.1016/j.ydbio.2009.10.026.
44. Khademhosseini A, Langer R. A decade of progress in tissue engineering. Nat Protoc. 2016. https://doi.org/10.1038/nprot.2016.123.
45. Pampaloni F, Reynaud EG, Stelzer EH. The third dimension bridges the gap between cell culture and live tissue. Nat Rev Mol Cell Biol. 2007. https://doi.org/10.1038/nrm2236.
46. Hauge-Evans AC, Squires PE, Persaud SJ, Jones PM. Pancreatic beta-cell-to-beta-cell interactions are required for integrated responses to nutrient stimuli: enhanced Ca2+ and insulin secretory responses of MIN6 pseudoislets. Diabetes. 1999. https://doi.org/10.2337/diabetes.48.7.1402.
47. Chowdhury A, Dyachok O, Tengholm A, Sandler S, Bergsten P. Functional differences between aggregated and dispersed insulin-producing cells. Diabetologia. 2013. https://doi.org/10.1007/s00125-013-2891-4.

48. Bae CY, Min MK, Kim H, Park JK. Geometric effect of the hydrogel grid structure on in vitro formation of homogeneous MIN6 cell clusters. Lab Chip. 2014. https://doi.org/10.1039/C4LC00230H.
49. Chao X, Zhao F, Hu J, Yu Y, Xie R, Zhong J, Huang M, Zeng T, Yang H, Luo D, Peng W. Comparative study of two common in vitro models for the pancreatic islet with MIN6. Tissue Eng Regen Med. 2023. https://doi.org/10.1007/s13770-022-00406-8.
50. Klochendler A, Caspi I, Corem N, Moran M, Friedlich O, Elgavish S, Nevo Y, Helman A, Glaser B, Eden A, Itzkovitz S, Dor Y. The genetic program of pancreatic β-cell replication in vivo. Diabetes. 2016. https://doi.org/10.2337/db16-0003.
51. Puri S, Roy N, Russ HA, et al. Replication confers β-cell immaturity. Nat Commun. 2018. https://doi.org/10.1038/s41467-018-02939-0.
52. Blanchi B, Taurand M, Colace C, Thomaidou S, Audeoud C, Fantuzzi F, Sawatani T, Gheibi S, Sabadell-Basallote J, Boot FW, Chantier T. EndoC-βH5 cells are storable and ready-to-use human pancreatic beta cells with physiological insulin secretion. Mol Metab. 2023. https://doi.org/10.1016/j.molmet.2023.101772.
53. Alessandra G, Algerta M, Paola M, Carsten S, Cristina L, Paolo M, Elisa M, Gabriella T, Carla P. Shaping pancreatic β-cell differentiation and functioning: the influence of mechanotransduction. Cells. 2020. https://doi.org/10.3390/cells9020413.
54. Galli A, Maffioli E, Sogne E, Moretti S, Di Cairano ES, Negri A, Nonnis S, Norata GD, Bonacina F, Borghi F, Podestà A. Cluster-assembled zirconia substrates promote long-term differentiation and functioning of human islets of Langerhans. Sci Rep. 2018. https://doi.org/10.1038/s41598-018-28271-4.
55. Nyitray CE, Chavez MG, Desai TA. Compliant 3D microenvironment improves β-cell cluster insulin expression through mechanosensing and β-catenin signaling. Tissue Eng Part A. 2014. https://doi.org/10.1089/ten.TEA.2013.0532.
56. Zhang M, Yan S, Xu X, Yu T, Guo Z, Ma M, Zhang Y, Gu Z, Feng Y, Du C, Wan M. Three-dimensional cell-culture platform based on hydrogel with tunable microenvironmental properties to improve insulin-secreting function of MIN6 cells. Biomater. 2021. https://doi.org/10.1016/j.biomaterials.2021.120687.
57. Mendelsohn AD, Nyitray C, Sena M, Desai TA. Size-controlled insulin-secreting cell clusters. Acta Biomater. 2012. https://doi.org/10.1016/j.actbio.2012.07.033.
58. Singh J. The national centre for the replacement, refinement, and reduction of animals in research. J Pharmacol Pharmacother. 2012
59. Gloyn AL, Ibberson M, Marchetti P, Powers AC, Rorsman P, Sander M, Solimena M. Every islet matters: improving the impact of human islet research. Nat Metab. 2022. https://doi.org/10.1038/s42255-022-00607-8.
60. Kulkarni RN, Stewart AF. Summary of the Keystone islet workshop (April 2014): the increasing demand for human islet availability in diabetes research. Diabetes. 2014; https://doi.org/10.2337/db14-1303
61. Abazari MF, Soleimanifar F, Aleagha MN, Torabinejad S, Nasiri N, Khamisipour G, Mahabadi JA, Mahboudi H, Enderami SE, Saburi E, Hashemi J. PCL/PVA nanofibrous scaffold improve insulin-producing cells generation from human induced pluripotent stem cells. Gene. 2018. https://doi.org/10.1016/j.gene.2018.05.082.
62. Enderami SE, Kehtari M, Abazari MF, Ghoraeian P, Nouri Aleagha M, Soleimanifar F, Soleimani M, Mortazavi Y, Nadri S, Mostafavi H, Askari H. Generation of insulin-producing cells from human induced pluripotent stem cells on PLLA/PVA nanofiber scaffold. Artif Cells, Nanomed and Biotechnol. 2018. https://doi.org/10.1080/21691401.2018.1443466
63. Takahashi I, Noguchi N, Nata K, Yamada S, Kaneiwa T, Mizumoto S, Ikeda T, Sugihara K, Asano M, Yoshikawa T, Yamauchi A. Important role of heparan sulfate in postnatal islet growth and insulin secretion. Biochem and Biophys Res Commun. 2009. https://doi.org/10.1016/j.bbrc.2009.03.140.
64. Messelmani T, Le Goff A, Souguir Z, Maes V, Roudaut M, Vandenhaute E, Maubon N, Legallais C, Leclerc E, Jellali R. Development of liver-on-chip integrating a hydroscaffold mimicking the liver's extracellular matrix. Bioeng. 2022. https://doi.org/10.3390/bioengineering9090443.